Complex Dynamics of Magnetic Billiards in a Torus

Albert Šilvans, s3400166

September 20, 2023

Contents

List of Figures

1 Introduction

Mathematical billiards is a broad topic in dynamical systems which studies the long term motion of a particle in the presence of an obstruction. The obstruction can be a boundary upon which the particle collides and then is elastically reflected, or there can be a vector field that deflects the particle, for example, a magnetic field. In this paper we consider the latter. We take the work [KS17] and [Gas21] as inspiration.

Let $H : \mathbb{R}^3 \times \mathbb{R}^3 \to \mathbb{R}$ be a magnetic Hamiltonian function:

$$H(q, p) = \frac{1}{2} \| p - A(q) \|^2 \tag{1}$$

where $q = (q_1, q_2, q_3)$ is position, $p = (p_1, p_2, p_3)$ is momentum, $A : \mathbb{R}^3 \to \mathbb{R}^3$ is a magnetic vector field defined as follows:

$$A(q) = (-b(q_2 \mod 1), 0, 0) \mathbb{1}_S(q \mod 1) \tag{2}$$

$$S = \{ x \in \mathbb{R}^2 : \| x - 1/2 \| \le R \}, \tag{3}$$

with magnetic field strength $b \in (0, \infty)$, and $R \in (0, 1/2)$, the radius of the disk S centered at $(1/2, 1/2)$ in the plane. Lastly, $\mathbb{1}_S$ is an indicator function on S, that is $\mathbb{1}_S(x) = 1$ if $x \in S$ and $\mathbb{1}_S(x) = 0$ otherwise.

We note that A is independent of q_3, so for $q_3 = p_3 = 0$, a solution of the Hamiltonian equations of H is contained within the $q_1 q_2$-plane. So, we ignore the q_3 variable completely. Furthermore, A is 1-periodic in both q_1 and q_2, so we can consider H on the torus $\mathbb{T} = \mathbb{R}^2 / \mathbb{Z}^2$ via the quotient. We will refer to H on either surfaces interchangeably. Likewise, the periodicity of A gives rise to a lattice of disks centered at the points $N + 1/2$ for $N \in \mathbb{Z}^2$, we use the variable S to refer to either the disc in $[0, 1]^2$ or to the lattice, and make it clear which we are referring to when necessary.

The motion of a particle under H in the interior and the exterior of S is well understood. In the exterior of S there is no magnetic field, so the particle experiences free motion and travels in a straight line. In the interior of S, we know that the particle travels along arcs of a *Larmor* circle with *Larmor* radius $\| p \| / b$. Since eq. (1) is discontinuous along the boundary ∂S, we have an issue when considering particles that enter ∂S tangentially, in which case the solution is not necessarily unique. In such cases, we assume the particle is in free motion.

We see an example trajectory in fig. 1 which demonstrates the types of motion exhibited by the system. In blue we indicate free motion, and in red we have motion in the magnetic field. The red segments should instead be circular arcs, we reserve some artistic liberty in this choice. We also only draw the boundary of disks that are hit by the particle, and skip the rest to improve legibility. Focusing now on the trajectory itself we see:

- erratic behavior, that is, the trajectory seems to bounce around in a chaotic manner;

- evidence for quasi-periodic motion, specifically referring to the spot where the particle is trapped between four discs before eventually escaping;

- two distinct scales, the intervals of magnetic motion serve as a perturbation or deflection and are rather local, while the intervals of free motion

can be long and in fact can be arbitrarily long provided that the particle exits a disc at a shallow enough angle.

Trajectory, $(X, V) \approx (0.632, 0.194, 1, 0), R \approx 0.33, b = 3$
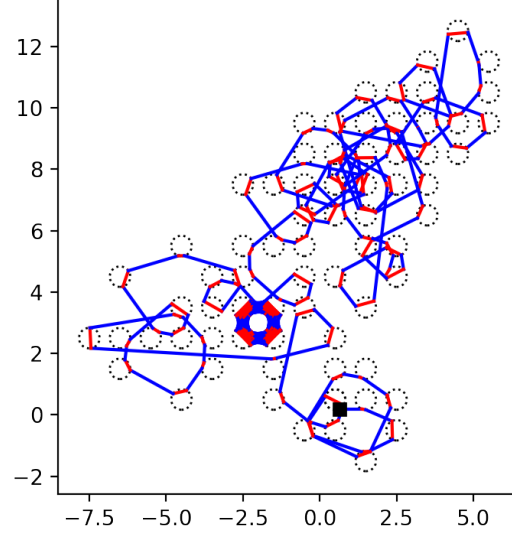
Figure 1: An example trajectory illustrating various types of motion.

So far, we see that the motion is not trivial, and warrants study. What is not yet evident from fig. 1 is the influence of the parameters R and b on the general behavior of the system. This is what we aim to better understand by the end of the paper.

We outline how we study this system. We focus on varying b, and identify three modes. For some $b_1, b_2 \in \mathbb{R}$ with $0 < b_1 \ll 1 < b_2$ we can also just suggest some values, given our observations,

1. If $0 < b < b_1$, the field strength is low. We can use KAM theory to make sense of quasi-periodicity at these strengths. We find two approaches using KAM.

2. If $b_1 < b < b_2$, the field has moderate strength and there is quasi-periodicity of varying complexity. We study this mode, and the next using symbolic dynamics and the Lempel-Ziv complexity measure.

3. If $b_2 < b$, the field is strong, and though periodic solutions can be found, we cannot find stable ones.

4

2 Weak magnetic fields and KAM theory

We begin by recalling Kolmogorov-Arnold-Moser (KAM) theory, state one of the main KAM theorems, and briefly outline the main points of the theory before delving into its application. We refer the reader to [Kna18] and [Ser22] for a more detailed account. We strongly recommend [Pö82] for reference, as it is the version of KAM we use here. What we will see is that for "small" values of b, our system (1) can be viewed as a perturbation of at least two different Hamiltonian systems, which can explain certain behavior we find. We corroborate our reasoning with many numerical simulations.

2.1 Summary of KAM theory

KAM theory is a method for studying perturbations of integrable Hamiltonian systems. Its origins lie in Celestial and Hamiltonian mechanics, where it was used to study the orbits of planets. Hamiltonian mechanics is a strong tool for modeling and studying systems, however it is strongest for conservative systems. Naturally, we find in practice many non-conservative systems, or conservative ones that are too complicated in full, in which case a smaller subsystem is modeled and the rest is viewed as a perturbation. We are interested in the second scenario, we denote by $H^0(q,p)$ an integrable Hamiltonian and by $H^1(q,p,\varepsilon)$ a perturbation.

Focusing on the integrable case, it is known by the Liouville-Arnold theorem that there exist *action-angle* coordinates so that $H^0 := H^0(p)$ can be expressed in terms of the action variable only. The equations of motion in action-angle coordinates are given by:

$$\dot{q} = \omega, \qquad \dot{p} = 0,$$

where $\omega = \partial_p H^0(p)$ and $\partial_p H^0 : I \to \Omega$ is the so-called *frequency map*. In these action-angle coordinates, the phase space becomes $\mathbb{T}^n \times I$ where $I \subseteq \mathbb{R}^n$ and the dynamics of the system are completely expressed as rotations on the torus. Specifically, phase space is foliated into a family of invariant tori $\mathbb{T}^n \times \{p\}$ for each $p \in I \subseteq \mathbb{R}^n$. We consider only integrable Hamiltonians with a *non-degenerate* frequency map, that is, $\det \partial_p^2 H^0 \neq 0$. Now, KAM deals with Hamiltonians of the form

$$H(q,p) = H^0(p) + \varepsilon H^1(q,p),$$

where $1 \gg \varepsilon > 0$ is considered small, H^0 is the integrable part and H^1 is the perturbation. We assume that H is 2π-periodic in each component of q. What KAM theory ensures is that under the correct conditions, a "large" subset $\Omega_{\gamma,\tau} \subseteq \Omega$, $\gamma, \tau > 0$ of invariant tori of $H^0(p)$ are preserved, though possibly deformed, under the perturbation H^1. The set $\Omega_{\gamma,\tau}$ is given by:

$$\Omega_{\gamma,\tau} = \bigcap_{\substack{k \in \mathbb{Z} \\ k \neq 0}} \left\{ \omega \in \Omega : |\omega \cdot k| \geq \gamma |k|^{-\tau} \right\}. \tag{4}$$

The condition for $\Omega_{\gamma,\tau}$ is called the *small divisor condition*. It can be shown for $\tau > n - 1$ that for almost all $x \in \mathbb{R}^n$ there exists a $\gamma > 0$ such that $x \in \Omega_{\gamma,\tau}$, so

in particular, we can find $\gamma > 0$ so that a point $\omega \in \Omega$ satisfies $\omega \in \Omega_{\gamma,\tau}$. We finally consider the *Cantor* set

$$\hat{\Omega}_{\gamma,\tau} = \Omega_{\gamma,\tau} \cap \{\omega \in \Omega : d(\omega, \partial\Omega) \geq \gamma\},$$

that is, we remove points in $\Omega_{\gamma,\tau}$ that have distance less than γ from the boundary of Ω. It can be shown $\Omega \backslash \bigcup_{\gamma>0} \hat{\Omega}_{\gamma,\tau}$ is a set of measure zero, so the measure of $\hat{\Omega}_{\gamma,\tau}$ becomes large for small γ ,justifying the term "large". We can now give the KAM theorem as stated in [Pö82].

Theorem 1. Let the integrable Hamiltonian $H^0 : \mathbb{T}^n \times I \to \mathbb{R}$ be real analytic and non-degenerate, such that the frequency map $\partial_p H^0 : I \to \Omega$ is a diffeomorphism and let the perturbed Hamiltonian $H = H^0 + \varepsilon H^1$ be of class $C^{\alpha\lambda+\lambda+\tau}$ with $\lambda > \tau + 1 > n$ and $\alpha > 1$. Then there exists a positive γ-independent δ such that for $|\varepsilon| < \gamma^2 \delta$ with γ sufficiently small, there exists a diffeomorphism

$$\mathcal{T} : \mathbb{T}^n \times \Omega \to \mathbb{T}^n \times I,$$

which on $\mathbb{T}^n \times \hat{\Omega}_{\gamma,\tau}$ transforms the equations of motion of H into

$$\dot{\theta} = \omega, \qquad \dot{\omega} = 0.$$

The map $\mathcal{T}$ is of class C^α for non-integer α and close to the inverse of the frequency map; its Jacobian determinant is uniformly bounded from above and below. In addition, if H is of class $C^{\beta\lambda+\lambda+\tau}$ with $\alpha \leq \beta \leq \infty$, then one can modify $\mathcal{T}$ outside $\mathbb{T}^n \times \hat{\Omega}_{\gamma,\tau}$ so that $\mathcal{T}$ is of class C^β for noninteger β.

So, for $\omega \in \hat{\Omega}_{\gamma,\tau}$, we parametrize an invariant torus via the map $\theta \mapsto \mathcal{T}(\theta, \omega)$. There are a few theorems in use now that are titled the *KAM theorem*, and they differ mainly whether they discuss analytic or smooth perturbations. It is easier to find sources discussing the analytic versions, since they provide stronger results about the invariant torii. Having said this, we use the C^r version because it is easier to construct smooth approximations of discontinuous functions as opposed to analytically approximating them. We bring smooth approximations into the mix, since (1) alone is discontinuous.

2.2 Approximating locally L^1 functions

The Hamiltonian (1) we wish to study is discontinuous, which by itself is not suitable for the KAM theorem. We can, however, smoothly approximate the Hamiltonian by using *mollifiers*. The KAM theorem then can be applied to the smoothed Hamiltonian, which of course means we are not directly studying (1) but instead gaining an intuition for the true behavior.

The *standard mollifier* $\varphi : \mathbb{R}^n \to \mathbb{R}$ is the following function:

$$\varphi(x) = \begin{cases} c \exp\left(\frac{1}{|x|^2-1}\right), & |x| < 1 \\ 0, & |x| \geq 1, \end{cases}$$

where $c > 0$ is a scaling factor chosen so that the integral of φ over $\mathbb{R}^n$ is 1. Also, φ is commonly called a *bump* function, since its support is compact. For $\varepsilon > 0$, let

$$\varphi_\varepsilon(x) = \frac{1}{\varepsilon^n} \varphi\left(\frac{x}{\varepsilon}\right),$$

this function has the following properties:

$$\varphi_\varepsilon \in C_c^\infty(\mathbb{R}^n), \quad \varphi \geq 0,$$

$$\int_{\mathbb{R}^n} \varphi_\varepsilon = 1, \quad \operatorname{supp}(\varphi_\varepsilon) \subset B_\varepsilon(0) = \{x \in \mathbb{R}^n : |x| < \varepsilon\},$$

that is, the function φ_ε is smooth in $\mathbb{R}^n$ with compact support, it is positive, its integral is 1, and the support of φ_ε is fully contained in the unit ball of radius $\varepsilon > 0$ centered at the origin.

Let $f \in L^1_{\mathrm{loc}}(X)$ be a locally integrable function in $X \subseteq \mathbb{R}^n$. The *mollification* of f is defined as the convolution of f with φ_ε, that is, $\varphi_\varepsilon * f : X_\varepsilon \to \mathbb{R}$ where $X_\varepsilon = \{x \in X : d(x, \partial X) > \varepsilon\}$. Explicitly,

$$f_\varepsilon(x) = (\varphi_\varepsilon * f)(x) = \int_X \varphi_\varepsilon(x - y)f(y)dy$$

$$= \int_{B_\varepsilon(0)} \varphi_\varepsilon(y)f(x - y)dy, \quad x \in X_\varepsilon$$

Some properties that the mollification f_ε has are summarized here:

Theorem 2. Let $f \in L^1_{\mathrm{loc}}(X)$. Then the mollification f_ε has the following properties:

1. $f_\varepsilon \in C^\infty(X_\varepsilon)$,

2. $f_\varepsilon \to f$ almost everywhere as $\varepsilon \to 0$,

3. if f is continuous on X, then $f_\varepsilon \to f$ as $\varepsilon \to 0$ uniformly on compact subsebts of X,

4. if $1 \leq p < \infty$ and $f \in L^p_{\mathrm{loc}}(X)$, then $f_\varepsilon \to f$ as $\varepsilon \to 0$ in $L^p_{\mathrm{loc}}(X)$

Proof. The proof of this theorem can be found in Appendix C of [Eva98] ∎

What we gain from Theorem 2 is not only a smooth approximation of our discontinuous Hamiltonian but an approximation that can be made arbitrarily precise almost everywhere. Of course, the points which cannot be approximated accurately are concentrated at the boundary of each disk, where the discontinuities lie. Despite this, it is reasonable to assume that for sufficiently small values of ε, the flow of the equations of motion provided by the mollified Hamiltonian approximate the flow of the disconitinuous one very well.

2.3 Investigating small magnetic field strengths

In fig. 2 we numerically solve the system and observe some interesting relations. Each plot shows 5 trajectories varying $b = 10^{-1}, \ldots, 10^{-5}$. In fig. 2a and fig. 2b the init. cond. and params. are the same $X \approx (0.38, 0.81)$ and $V \approx (0, 1)$, and $R = 1/3$, only the duration of the simulation is longer in fig. 2b. In fig. 2c, V is the same, $X \approx (0.44, 0.65)$ and $R = 1/6$.

First, we see in each figure the trajectory for $b = 0.1$ appears as a smear near the origin, this is likely because b is large enough for the deflection in each disk to be significant. We note, however, in later sections we also find circle-like quasiperiodic trajectories for significantly larger values of b. The difference here

is that these circular arcs seem to be generic, while for larger b the circle-like trajectories are more scarce and each has a smaller region of stability.

For the other values of b, we see the trajectories follow a circular arc, and for smaller b the radius of the respective circular arc is larger. In the limit $b \to 0$, the trajectories will straighten out, since the magnetic field vanishes. These two observations motivates the use of KAM, specifically, considering (1) as a perturbation of either free motion or of a uniform magnetic field in the plane.
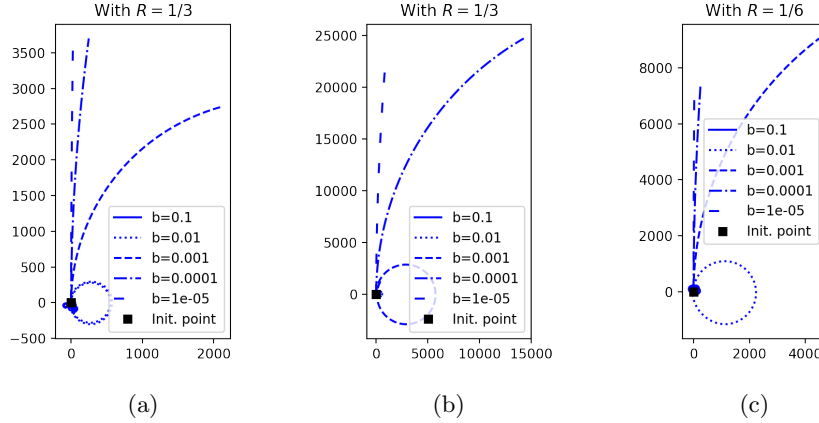

Figure 2: Trajectories for various choices of R and small b.

We note that the free motion perturbation idea seems to be less robust than the uniform field idea. For any small $b > 0$, we can expect that after a sufficiently long time t the accumulated deflection is substantial, for example, compare the trajectory for $b = 0.0001$ in fig. 2a and fig. 2b. Having said that, it is not visible in the figure but what appear as circular trajectories in fact do not close either, the displacement is simply very small, but this is precisely what motivated the previous comment: the circles stay circular for longer.

2.4 Perturbations of linear motion

Recall, that a particle in the plane moves along Larmor circles when in the presence of a uniform magnetic field, with strength b, orthogonal to the plane of motion. The Larmor radius R depends inversely with respect to the field strength, $Rb \propto 1$, that is, a weaker the field strength corresponds to a larger Larmor radius. So, as $b \to 0$, we expect $R \to \infty$, which means that locally the trajectory approaches linear motion in the plane. This intuition is coroborated when considering the Hamiltonian (1) and setting $b = 0$. Hence, it is natural to consider the Hamiltonian $H_0(q, p) = \|p\|^2/2$ and perturb it.

We see H_0 is real analytic, it is also in action-angle coordinates from which we can deduce it is non-degenerate $\det \partial_p^2 H_0 = 1 \neq 0$, and the frequency map $\partial_p H_0(p) = p$ is a diffeomorphism. Now, we attempt to isolate H_0 in (1) from

the perturbation term. Writing $A = (A_1, A_2, A_3)$, we see:

$$H(q, p) = \frac{1}{2} \|p - A(q)\|^2 = \frac{1}{2} (p_1 + A_1(q))^2 + \frac{1}{2} p_2^2$$

$$= \frac{\|p\|^2}{2} + \frac{1}{2} \left(2p_1 A_1(q) + A_1^2(q) \right)$$

$$\stackrel{(\star)}{=} H_0(p) + bH_1(q, p, b)$$

where in $(\star)$ we used that we can factor out b from $A_1(q)$. As previously discussed, H_1 is discontinuous, so to apply KAM, we need to mollify H_1. Hence, consider the mollified perturbation $\hat{H}_1 = \varphi_\varepsilon * H_1$, where $\varepsilon > 0$ is a parameter independent of b. Now, by Theorem 1, for sufficiently small $b > 0$ there are tori of H_0 that are preserved under the perturbation H_1.

2.5 Perturbation of motion in a constant field

We first reason heuristically to see that this idea is valid. Comparing the trajectories for $b = 0.01$ and 0.001 in fig. 2a and 2b, we see that the radius of the trajectory is ≈ 250 and ≈ 2500, respectively. If we assume this is the value of the Larmor radius $\hat{L}$ in each case, then we see $\hat{L} \propto 1/b$ or $\hat{b} \propto b$. Now, comparing the trajectories for $b = 0.01$ in fig. 2a and 2c, we see halving the radius R of the magnetic bumps roughly quadruples the radius $\hat{L}$ from 250 to 1000, that is, $\hat{L} \propto 1/R^2$, and the strength then relates as $\hat{b} \propto R^2 b$. The task then is to determine $C \in \mathbb{R}$ such that $\hat{b} = CR^2 b$.

We can reason another way. Focusing on $[0, 1]^2$, we would like the uniform field $\hat{\mathbf{B}} = \nabla \times \hat{A} = (-\hat{b}q_2, 0, 0)$ to deflect trajectories as would $\mathbf{B} = \nabla \times A$. How much a trajectory is deflected depends on the flux of the field, since the flux measures the "flow" of the field through a surface. Equating the fluxes $\Phi_\mathbf{B} = \Phi_{\hat{\mathbf{B}}}$, we can compute the required strength $\hat{b}$ for $\hat{B}$. The flux of $\mathbf{B}$ through a bounded region in the plane is given by:

$$\Phi_\mathbf{B} = \iint_S \mathbf{B} \cdot dA = \iint_S \nabla \times A \cdot dA = \iint_S (0, 0, b) \cdot (0, 0, 1) dA = bA(S),$$

where $A(S)$ denotes the area of the surface. In our case, $\Phi_{\hat{\mathbf{B}}} = \Phi_\mathbf{B}$ implies $\hat{b} = \pi R^2 b$, which is about what we expected. Now, we should numerically test this hypothesis. To test the validity of the relation, we give two tests, the results of which can be found in fig. 3. The first test:

1. For $1 \leq i \leq 50$, sample (R_i, b_i) uniformly from $[0.25, 0.45] \times [10^{-10}, 10^{-6}]$

2. For R_i, b_i uniformly sample initial conditions X_{ij}, V_{ij} with $1 \leq j \leq 20$.

3. Using the method in [Coo93], fit a circle to the trajectory of each X_{ij}, V_{ij}, the radius of which is $\hat{L}_{ij}$. We take the average $\hat{L}_i = \sum_{j=1}^{20} \hat{L}_{ij}/20$.

4. Via a least squares method, we fit a general cubic:

$$a_0 + a_1 R_i + a_2 b_i + a_3 R_i^2$$
$$+ a_4 R_i b_i + a_5 b_i^2 + a_6 R_i^3 + a_7 R_i^2 b_i + a_8 R_i b_i^2 + a_9 b_i^3 = 1/\hat{L}_i.$$

The second test is similar, we fix $R_i = 1/3$, and fit a line $a_0 + a_1 R_i^2 b_i = 1/\hat{L}_i$. We opt to fit a general cubic function to avoid any bias in reasoning. We should expect after fitting that only a_7 contributes significantly.

The coefficients of the fitted cubic surface in fig. 3a come out to

$$a_0 \approx 6.7 \cdot 10^{-8}, \qquad a_1 \approx -6.2 \cdot 10^{-7}, \qquad a_2 \approx 6.7 \cdot 10^{-3},$$
$$a_3 \approx 1.9 \cdot 10^{-6}, \qquad a_4 \approx -5.3 \cdot 10^{-2}, \qquad a_5 \approx -1.9 \cdot 10^{+2},$$
$$a_6 \approx -1.8 \cdot 10^{-6}, \qquad a_7 \approx 3.2, \qquad a_8 \approx -6.6 \cdot 10^{+1},$$
$$a_9 \approx -3.0 \cdot 10^{-4},$$

the values of a_0 to a_4, a_6 and a_9 are negligible as expected, likewise $a_7 \approx \pi$. We notice that a_5 and a_8 are quite large but we reason that the contribution of their respective monomial term is still small, since both contain a factor of b^2 which has an order of magnitude at most 10^{-6}. The coefficients of the fitted line in fig. 3b are $a_0 \approx 4.4 \cdot 10^{-10}$ and $a_1 \approx 3.12$, which can be explained in the same way. So, the relation $\hat{b} = \pi R^2 b$ seems valid, and this motivates perturbing a uniform magnetic field into the bump field.
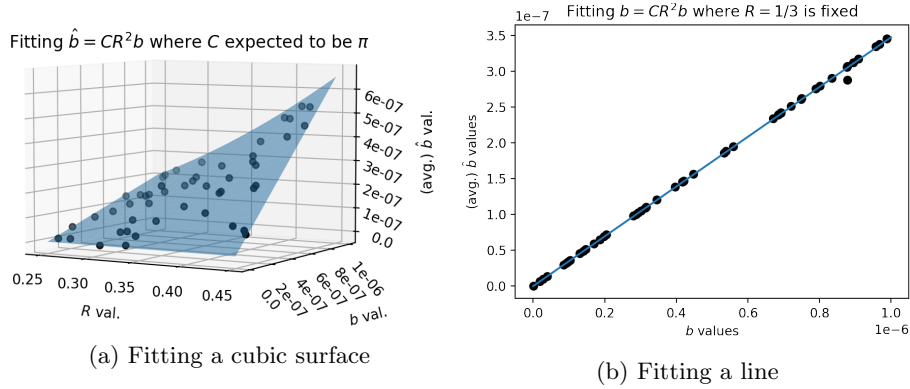

(a) Fitting a cubic surface

(b) Fitting a line

Figure 3: Plots of data and fitted polynomial models.

Overall, the results show that our assumptions are plausible, we approximately see π in the coefficient. The results are not as precise as desired but that can be due to randomly choosing the initial conditions for the trajectories. The circular trajectories correspond to invariant tori, and since not all tori are preserved under the perturbation, we expect that, chosen at random, some trajectories will not follow closely a circular path. Similarly, the chosen range for sampling R and b could be too large, though in tests we made that we omit here, we noticed that the relation holds more or less for a wider range of $[0.1, 0.45] \times [10^{-16}, 10^{-2}]$.

3   Complexity and symbolic dynamics

In this section we consider the dynamics of (1) for $b \gg 0$, that is, in the case where KAM and perturbative methods are not readily applicable. We approach the system in an exploratory way: we look for (quasi)-periodic orbits, consider their stability, and see where stability is missing.

To this end, we prove the existence of a Poincaré section, later we induce "coarse" symbolic dynamics and apply the Lempel-Ziv complexity to make sense of the dynamics. What we find is rich dynamics and a visual method of analysis well suited for similar problems.

The phase space of our system is $\mathbb{R}^2 \times \mathbb{R}^2$, however we can reduce the phase space to a Poincaré section as follows:

Proposition 1. Let S be the union of discs of radius R centered at $\mathbb{Z}^2 + 1/2$. The sets S_{in} and S_{out} defined as:

$$S_{\text{in}} = \bigcup_{x \in \partial S} \{x\} \times \{v \in \mathbb{R}^2 : v \cdot (x - 1/2) < 0\}, \tag{5}$$

$$S_{\text{out}} = \bigcup_{x \in \partial S} \{x\} \times \{v \in \mathbb{R}^2 : v \cdot (x - 1/2) > 0\}, \tag{6}$$

are Poincaré sections for the system (1).

We prove this later. This helps visualize long term behavior, since the magnitude of the velocity of a trajectory is constant. Furthermore, we can pass the system to the torus, which reduces S to one disc. So, when plotting we only need two dimensions: one to parametrize ∂S and another for the velocity.

3.1   First impressions and lots of quasiperiodicity

For the remainder of this section we fix $R = 1/3$ and $\|p\| = 1$, we only vary b. In the figures below, we collect a few periodic and quasi-periodic orbits. For each figure, on the left is a plot of the trajectory in the plane, and on the right we give the trajectory restricted to the section S_{out}. The depth of computation is 2000 entries into S_{out}, unless stated otherwise. We discovered the trajectories in fig. 4 on paper, the rest were discovered using the methods we discuss later.
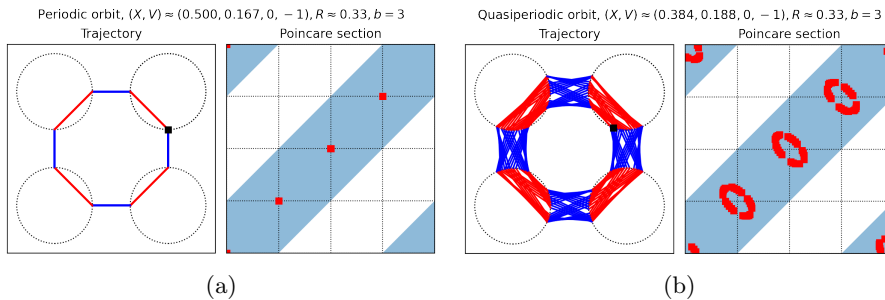

Figure 4: Stable trajectories discovered analytically (more on next page).

The trajectories fig. 4a, 4c, 4e, and 4f are periodic. Figure 4a and 4c are stable, we prove this in the python notebook [??], and 4b and 4d are given by
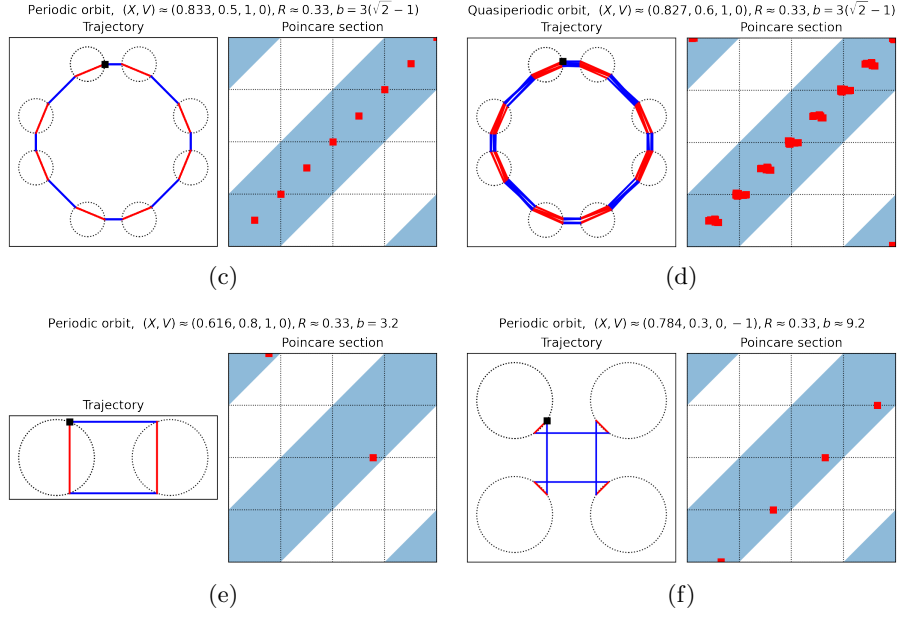
11

Figure 4: Unstable trajectories discovered analytically.

perturbed initial conditions of each case, respectively. Meanwhile 4e, 4f are unstable, in fact, the plots are given only to 35 iterations due to sensitivity.
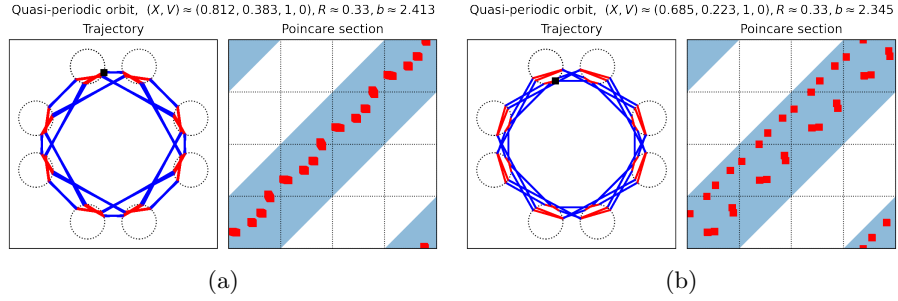

Figure 5: First signs of intricate quasi-periodicity.

Figure 5a and 5b are interesting, since they have a similar shape. The latter seems to be a "doubled" version of the former, and not a perturbation, since even after 2000 iterations the trajectory of 5b does not change, e.g., it does not smear like in the case of 4b.
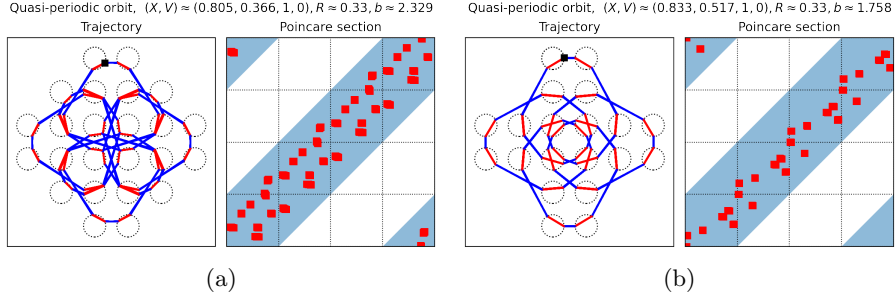
Figure 6: Complex and ornamental quasi-periodic trajectories.

Figure 6a and 6b are surprisingly complex patterns, and unlike the rest of the examples, involve the most discs in the plane
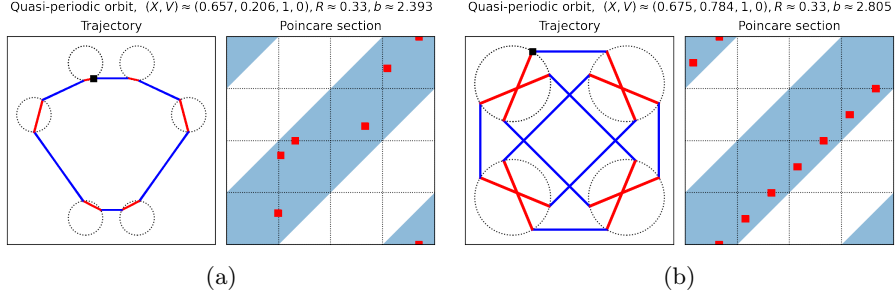

Figure 7: A symmetry breaking trajectory and an honorable mention.

So far, we have seen trajectories that have square symmetries, the first to break this is 7a with a bottom-heavy hexagon. It would be interesting to see if there are other polygon, for example triangles or pentagons. Figure 7b does not illustrate anything new, we included it because it is aesthetically pleasing.
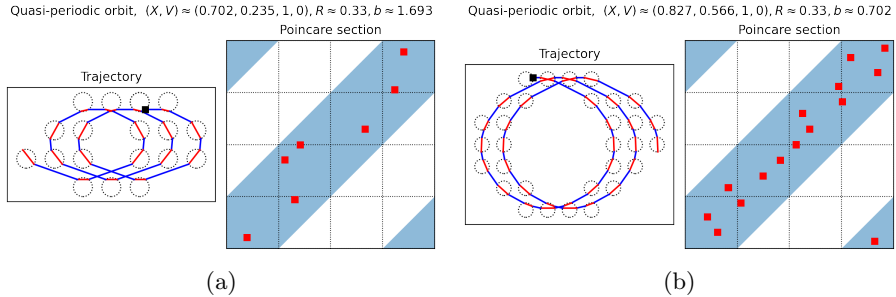

Figure 8: Wandering in $\mathbb{R}^2$, yet quasi-periodic in $\mathbb{T}$.

In fig. 8a and 8b we have the first examples of trajectories that wander in the plane but are quasi-periodic in the torus. It seems that these patterns arise in between values of b that produce trajectories as in fig. 9, that is, as b decreases,

the radii of the circles in the pattern increases, and if, in a specific way, the circle does not close, you can still see repetition.
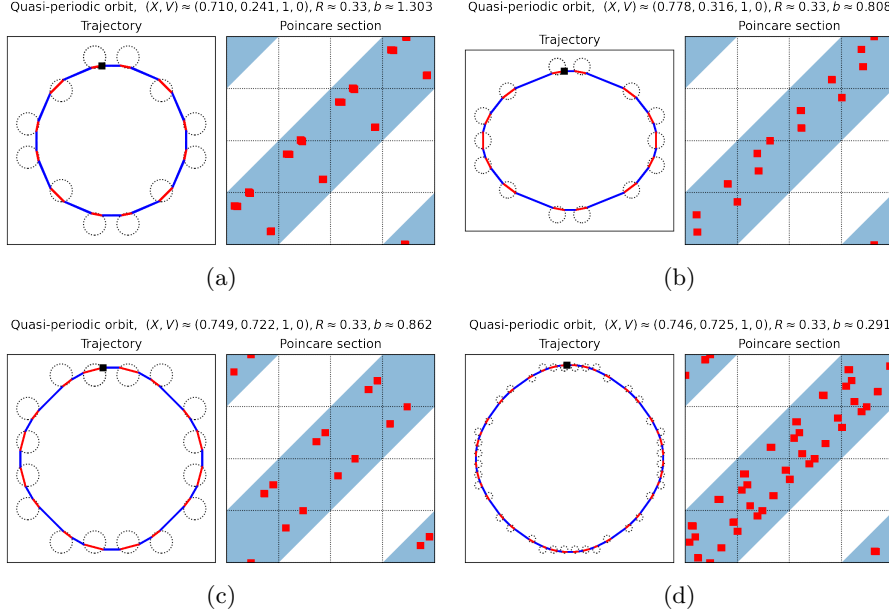

Figure 9: Large circular trajectories for small values of b.

The last 9a - 9d are examples with values of b relatively small compared to the rest. The lower the value of b, the closer the shape resembles a circle, which is in line with what we had seen using KAM. We have not found any intricate patterns for low values of b.

We see that in this simple system there is interesting dynamics with varying levels of complexity. It is safe to say that at least some of these would be hard to find by hand, and would be feasible only with some numerics and a measure of complexity for determining good candidates. We now construct the Poincaré section S_{in} and after that we outline the methods we used to obtain these quasi-periodic trajectories.

3.2 Constructing a Poincaré section

To construct the Poincaré section, we will use well known results about rotations on the torus. Parametrize the torus $\mathbb{T}$ with angles $\theta, \varphi \in [0, 1]$, a particle in free motion on $\mathbb{T}$ follows the trajectory $r(t) = x_0 + vt$ where $x_0 \in \mathbb{T}$ is the initial condition and $v \in \mathbb{R}^2$ is the velocity. If the angle of v with respect to the axis θ is rational, then $r(t)$ is periodic, otherwise $r(t)$ is dense in $\mathbb{T}$.

Lemma 1. The flow of (1) induces a well-defined map $P_{\text{oi}} : S_{\text{out}} \to S_{\text{in}}$.

Proof. Let $(x, v) \in S_{\text{out}}$, at this point the solution of (1) continues with free motion $r(t) = x + vt$. If the angle of v is rational, then there exists some time t_2 at which $r(t_2) = x$, and $(r(t_2), v) \in S_{\text{out}}$. Since at time t_2 the trajectory intersects ∂S transversally, there must exist $t_1 < t_2$ such that $(r(t_1), v) \in S_{\text{in}}$.

14

Since the trajectory intersects S_{in} at least once, there must exist a unique $t_0 \leq t_1$ such that $(r(t_0), v) \in S_{\text{in}}$.

If instead the angle of v is irrational, consider an open neighborhood $U \subseteq \partial S$ of x such that $U \times \{v\} \subseteq S_{\text{out}}$. This can be done by taking a sufficiently small interval in ∂S around x. Since $r(t)$ is dense in $\mathbb{T}$, there exists a time t_1 such that $r(t_1) \in U$. By the same reasoning as in the previous case, there exists a unique time t_0 such that $(r(t_0), v) \in S_{\text{in}}$.

Define $P_{\text{o}i}(x, v) = (r(t_0), v)$, which is well-defined. $\blacksquare$

Lemma 2. The flow of (1) induces a well-defined map $P_{\text{io}} : S_{\text{in}} \to S_{\text{out}}$.

Proof. Let $(x, v) \in S_{\text{in}}$, under the flow of (1) the trajectory $r(t)$ follows some Larmor circle C. We know $x \in C \cap \partial S$, so since (x, v) is transversal to ∂S, there must exist a point $x_1 \in C \cap \partial S$ with $x_1 \neq x$. Hence, also there must exist a time t_0 at which the trajectory intersects S_{out}. Define $P_{\text{io}}(x, v) = (r(t_0), r'(t_0))$. $\blacksquare$

Proof of proposition 1. The map $P_{\text{i}} = P_{\text{o}i} \circ P_{\text{io}}$ is a return map for S_{in}. Likewise, $P_{\text{o}} = P_{\text{io}} \circ P_{\text{o}i}$ is a return map for S_{out}. $\blacksquare$

The proof of lemma 1 does not depend on the shape of the magnetic region. However, it is not clear what needs to be changed to make lemma 2 work for arbitrary regions.

In [KS17] a similar result is proved for a configuration of finitely many bumps. In that case a different method was used that did not rely on an infinite number of bumps, in ours the reasoning was simplified due to this.

3.3 Mapping the Poincaré section to a Shift space

To study a discrete dynamical system in terms of symbolic dynamics one usually deduces a Markov partition of the space such that the system in question can be related via a (semi)-conjugacy to a shift-space of finite type. What is obtained is a simpler representation encoding the original dynamics. In the previous section, we successfully reduced the dynamics of (1) to a discrete system on either S_{in} or S_{out}. From now on we focus only on S_{out}.

A first attempt at establishing symbolic dynamics in our case runs into a few issues. Firstly, the shift map is continous on a shift-space, so provided S_{out} has the natural product topology, the map $P_{\text{o}} : S_{\text{out}} \to S_{\text{out}}$ should be continuous as well. Recall, $P_{\text{o}} = P_{\text{io}} \circ P_{\text{o}i}$, the map P_{io} can be shown to be continuous, however $P_{\text{o}i}$ is definitely not continuous. It is not clear a priori whether P_{o} is continuous, there could exist values of b which make it so. However, it is reasonable to assume that in general P_{o} is discontinuous. So, we should find a different topology on S_{out} for this method to work.

Next, it seems constructing a Markov partition is difficult. In the construction, we need to consider the stable and unstable sets of points in S_{out} under iteration of P_{o}, and by definition P_{o} must be at least differentiable, which we know it is not. Ignoring this issue, we can look for any reasonable partition that does not have the Markov property.

A reasonable partition should be finite, this way we can salvage some intuition from the above method. Focusing on the effects of $P_{\text{o}i}$, we see that, with the right conditions, a trajectory could jump to one of an infinite number of other circles relative to the circle we start from. So, to have a finite partition,

some concessions must be made. We could partition in such a way that jumps to a circle past a certain radius are all assigned the same symbol. One could also partition the circle lattice in a checkerboard fashion, yet neither of these approaches seem "natural". Hence, given all the resistence, we should consider another approach to symbolic dynamics.

Let $a_0 = (\theta_0, \varphi_0) \in S_{\text{out}}$, and define $a_n = P_o^n(a_0)$, that is, a_n is the n-th iterate of a_0. In the plane, each circle of S_{out} is associated with a coordinate $\mathbb{Z}^2 + 1/2$, then to each a_n we associate the coordinate s_n of the circle which a_n is on. Now, to the sequence of iterates $\{a_n\}_{n \geq 0}$ we associate the sequence of symbols $\{s_n - s_{n-1}\}_{n \geq 1} \subseteq \mathbb{Z}^2$. In other words, the symbols encode the relative jumps of the trajectory. Immediately, we notice that the alphabet we picked is countably infinite which we previously asserted was not *reasonable*, however we argue that this choice makes the least assumptions and hence in a sense is natural. Our choice will be further justified once we introduce the Lempel-Ziv complexity of strings.

3.4 The Lempel-Ziv compression algorithm

We introduce the Lempel-Ziv complexity (LZC) as described in [LZ76]. LZC operates on finite length sequences of symbols by applying a compression algorithm, the complexity of the original sequence is then quantified by the result of the compression.

We find it easiest to include the code of the implementation. The code is provided by Mediano and Rosas [MR19] and they attribute the implementation to [KS87] which is a nice use case and provides a good example of the algorithm.

```python
def LZ76(ss):
    """
    Input: ss -- array of integers
    Output: c  -- integer
    """
    i, k, l = 0, 1, 1
    c, k_max = 1, 1
    n = len(ss)
    while True:
        if ss[i + k - 1] == ss[l + k - 1]:
            k = k + 1
            if l + k > n:
                c = c + 1
                break
        else:
            if k > k_max:
                k_max = k
            i = i + 1
            if i == l:
                c = c + 1
                l = l + k_max
                if l + 1 > n:
                    break
                else:
                    i = 0
                    k = 1
                    k_max = 1
            else:
                k = 1
    return c
```

Loosely, we have two pointers ascending through the list, the left pointer is at index $i + k - 1$, and the right pointer is at index $\ell + k - 1$, at each iteration the pointers move depending on what symbol they see at their index. If they see the same symbol, the size of the window k is incremented by 1, so both pointers shift, if not then i is incremented by 1, i.e., only the left pointer shifts. As this happens we update the longest window size $k_{\max}$ that we encounter, this corresponds to the size of the longest word that can be reconstructed starting at index ℓ using only the words that appear before ℓ. Once $i = \ell$, we increment the number of words, the right pointer is pushed forward by $k_{\max}$, that is, ℓ becomes $\ell + k_{\max}$. The process repeats until the right pointer reaches the end of the list or if the current window size looks past the end of the list.

We provide examples below. The $\cdot$ is used as a word delimiter, the underline indicates the window at the left pointer, and the overline indicates the one at the right pointer. We only show the longest window that was achieved, notice the index of the longest window is not necessarily unique, and the window ends at the first symbol that differs.

$$01011010001101110010 \xrightarrow{(1)} \underline{0} \cdot \overline{1}011010001101110010$$

$$\xrightarrow{(2)} \underline{0} \cdot 1 \cdot \overline{01}1010001101110010$$

$$\xrightarrow{(3)} \underline{0} \cdot 1 \cdot 011 \cdot \overline{0100}011101110010$$

$$\xrightarrow{(4)} 0 \cdot 1 \cdot \underline{011} \cdot 0100 \cdot \overline{01101}110010$$

$$\xrightarrow{(5)} 0 \cdot 1 \cdot 011 \cdot 0\underline{100} \cdot 011011 \cdot \overline{10010}$$

$$\xrightarrow{(6)} \underline{0 \cdot 1} \cdot 011 \cdot 0100 \cdot 011011 \cdot 1001 \cdot \overline{0}\,,$$

the number of words is 7, so the LZC of this sequence is 7. Let's consider another example with repetition:

$$01101101101101101101 \xrightarrow{(1)} \underline{0} \cdot \overline{1}101101101101101101$$

$$\xrightarrow{(2)} 0 \cdot \underline{1} \cdot \overline{10}1101101101101101$$

$$\xrightarrow{(3)} 0 \cdot \underline{1} \cdot 10 \cdot \overline{1101101101101101}\,,$$

the number of words is 4, so the LZC is 4. Notice how the two examples have the same number of digits but the one with less repetition has greater complexity. We consider one final example:

$$01010101010101010101 \xrightarrow{(1)} \underline{0} \cdot \overline{1}010101010101010101$$

$$\xrightarrow{(2)} \underline{0} \cdot 1 \cdot \overline{010101010101010101}\,,$$

and we see the LZ complexity is 3. Notice that even though the last two examples are periodic, one has greater LZC, since the repeating word 011 is longer than 01. So, LZC not only differentiates between periodic and aperiodic sequences, it also distinguishes between periodic sequences of different period.

All examples were with the alphabet $\{0, 1\}$ but this can be done with an arbitrary alphabet. It's interesting to note that LZC also supports infinite

alphabets. Since we consider finite sequences, there is an upper bound for LZC, namely, the length of the sequence. We have yet to find a drawback in the setup.

The LZC is suited for comparing sequences of the same length. We can see this is the case by comparing 010 and 010101..., the latter can be made arbitrarily long and the two LZC will be still the same. Yet, this is meaningless, since the LZC of a short sequence will be comparable to its length.

Now, suppose we consider sequences generated by (1) using the procedure as discussed in the previous section. In this case the sequences encode information about trajectories of a dynamical system. We can apply LZC to these sequences to distinguish between periodic and aperiodic trajectories, though, since we use LZC for finite length sequences, we only compare trajectories up to a finite time horizon. Many structures in dynamical systems rely on infinite times, for example, limit cycles, so LZC may or may not detect them. Likewise, there exist systems with trajectories that can stay close to limit cycles for arbitrarily long times before diverging, so LZC could not detect this behavior unless a longer time horizon is chosen.

In fact, we see this type of behavior in fig. 1: if we took symbols up until the trajectory just jumped out from the 4 bumps, then the LZC would be very low for the length of the sequence, yet clearly the trajectory is not quasi-periodic. Focusing on the trajectories in fig. 2, we see that another issue can arise: the chosen time horizon could be shorter than the period of the (quasi)-periodic trajectory, LZC could label such a trajectory as complex despite the "macroscopic" structure that is apparent with the human eye. LZC would also struggle with eventually periodic sequences, if the periodic behavior arrives too late, then the LZC ranks the trajectory complex.

3.5 Lempel-Ziv varying b and initial conditions

In this section we focus on fig. 10, 11, and 12 which we used to find the quasi-periodic orbits we showed in a previous section. To create fig. 10 we computed trajectories for varying initial conditions and parameter b, specifically, we computed the trajectories for:

$$\left(\frac{1}{2} + \sqrt{R^2 - \left(y - \frac{1}{2}\right)^2}, y, 1, 0 \right) \text{ for } y \in \frac{1}{2} + 0.32 \cdot [-1, 1],$$

$$\text{and } b \in [0.001, 5],$$

where we sampled y and b in 500 equidistant points, and the trajectories were computed to a depth of 128 iterations. For fig. 11 we did the same except we varied $b \in [0.1, 1]$. The color in the plots indicates the LZC of the sampled trajectory. From the colorbar on the right, we see blue indicates low LZC, red intermediate, and yellow high LZC. The colors are scaled between the lowest and highest LZC in the plot, so colors in separate plots may vary. Also, notice the colorbar is scaled logarithmically, this improves legibility.

We immediately notice large regions of uniformly low LZC scattered across the plots, these suggest regions of stable quasi-periodic behavior. This is corroborated by the fact that in fig. 10 the trajectory for $(y, b) = (1/2, 3)$, corresponding to the periodic orbit in fig. 4a, lands inside one of these low LZC regions, and far from the boundary. In fact, the initial conditions for all of the quasi-periodic orbits we discovered can be found in either of these plots.
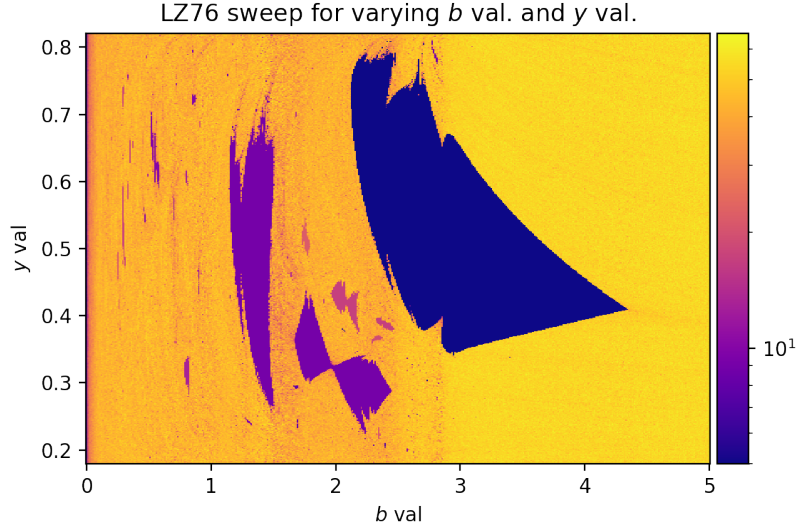
Figure 10: LZC for a 2-d slice of initial conditions

We note the color of the regions differs, indicating that the behavior producing the regions is qualitatively different. The regions do not seem to be arranged in any specific pattern, yet they all seem to have a similar structure: that being 1, 2, or 3 "bulbs". It might be that the number of bulbs may change depending on the resolution of the plot and depth of the interations. Figure 11 also suggests quasi-periodic trajectories exist for a large range of b, also for b in the range of our KAM results.
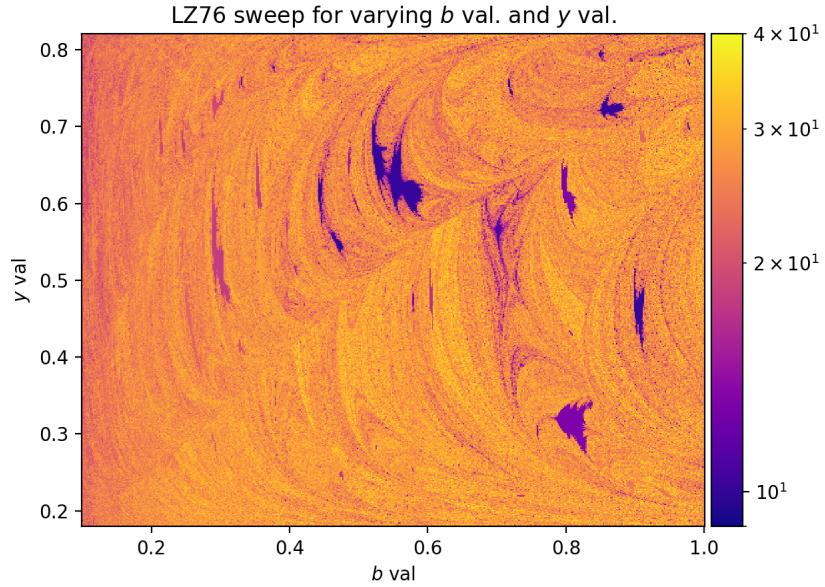

Figure 11: LZC for a narrower 2-d slice of initial conditions

19

If we repeat the same analysis for smaller b, the details are harder to discern. Focusing on $b \in (0.2, 0.4)$ in fig. 11, we still see the stable regions as before, however the color blends with the surrounding noise. This can be explained by the effect mentioned: the period of the trajectories is comparable to the time horizon, so periodicity is less distinguishable from noise.

Lastly, we discuss the boundary of the regions. Note that for $b \in (2, 3)$ and $y \in (0.7, 0.8)$ the plot seems grainy, in fact, zooming in, we find fractal-like behavior which can be seen in fig. 12. This is in contrast to the rest of the boundary which seems differentiable. We do not provide a figure but zooming in on the boundary for $b \in (3, 4)$ we see it is also grainy. It is not clear whether the noise is due to intrinsic structure or precision error.
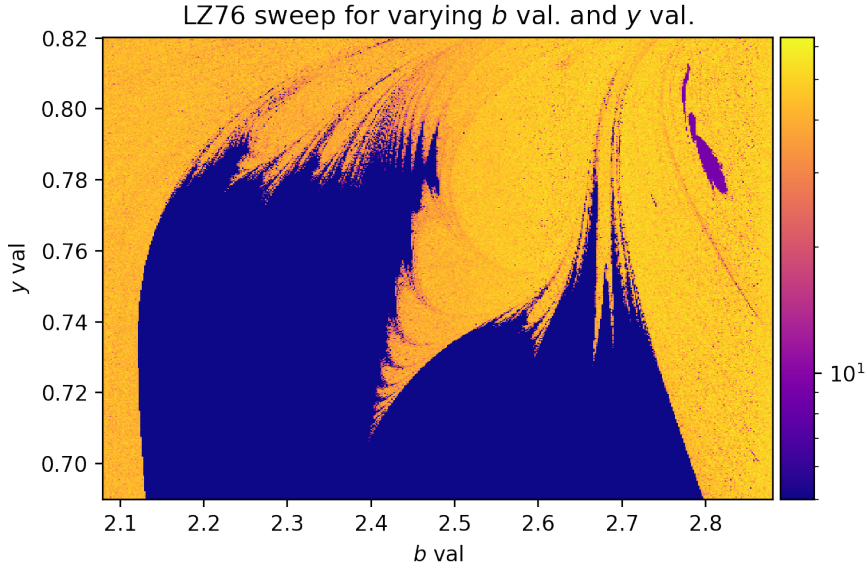

Figure 12: Fractal-like structure arising from Lempel-Ziv complexity

Apart from regions of stability, there is a sea of high and noisy LZC throughout the plots. Closer inspection shows specks with low LZC, it is not clear whether these specks are trajectories like fig. 1 or if they correspond to quasi-periodic regions with a very small radius of stability. Focusing on fig. 10, there is a peculiar vertical line at $b \approx 2.8$. On the right of this line the average LZC looks higher than to the left, we are curious whether there is any significance to this or if it is just a coincidence. Lastly, we also checked the plot for $b \in (5, 10)$ and found the same behavior as $b \in (4.3, 5)$: high LZC with no stable regions.

Using symbolic dynamics together with LZC we have probed a rich landscape of behavior. The choice of initial conditions and parameters for the above figures was deliberate, so it is interesting to ask whether we can expect a similar landscape for other choices. For example, will the view change if we vary velocity at a point, or if we pick a different radius $R \neq 1/3$. There are many option, and we invite the reader to explore as well.

3.6 Lempel-Ziv Poincaré sections for fixed b

A commonn method of analyzing dynamical systems is plotting a trajectory's return to a Poincaré section. In some cases one can also use it to prove the existence of a limit cycle or chaotic behavior. When it comes to visualization, one can only plot a handful of different trajectories in a Poincaré section before the image becomes too busy and illegible, so we see the details of a selection of trajectories and not the full picture.

We propose to apply a similar procedure for Poincaré sections as in the previous section: fix a value for b, and sample initial conditions on the Poincaré section, and compute LZC for each. If the resolution and depth of iteration is high enough. In such a way, we achieve a general picture of the dynamics.

Recall, the Poincaré section is parametrized by two angles θ and φ, the former is for the position, and the latter for the direction of the velocity. We fixed the speed to be 1. We only consider $\theta \in [-\pi/4, \pi/4]$, that is, only the right "side" of the circle S_{out}. We do not lose information doing this, since system eq. (1) has 4-fold rotational symmetry due to the lattice arrangement of the magnetic discs. The lattice is invariant under all square symmetries, but since the magnetic field always turns trajectories to the right, we cannot use reflections to further shrink the window to plot.
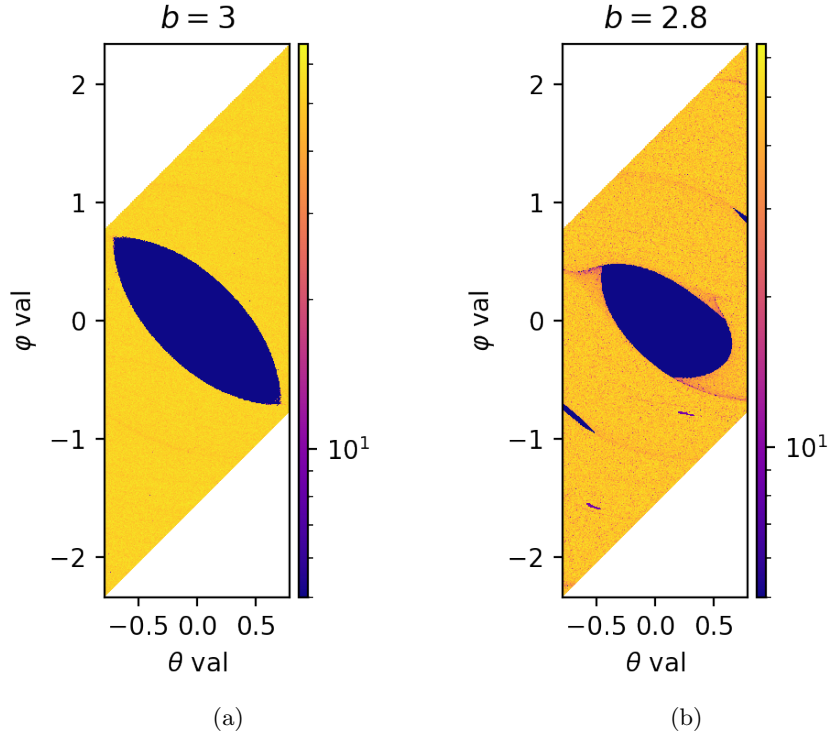

Figure 13: LZC plot of a few Poincaré sections

In fig. 13a, we again focus on $b = 3$, which has the periodic trajectory fig. 4a. The dynamics appears to be simple, there is a large region of quasi-

21

periodic trajectories around $(\theta, \varphi) = (0, 0)$, and the rest is uniformly high LZC. In fig. 13b, we perturb $b = 2.8$, the stable region from 13a changed shape, it is smaller, and there are now more noticeable artifacts along the boundary. Besides that, we see new stable regions: one larger, and two small. The two small ones likely belong to the same quasi-periodic trajectory, while the larger region belongs to its own. Looking back at fig. 7b, since there we had $b = 2.805$, we see indicated a periodic trajectory along the bottom edge of the Poincaré section. Here, we expect a similar trajectory, perhaps slightly perturbed. It's interesting to note that in fig. 13a we see faint streaks in the same spots where there are stable regions in fig. 13b. We conjecture that the patterns and streaks in the noise suggest a nearby bifurcation.
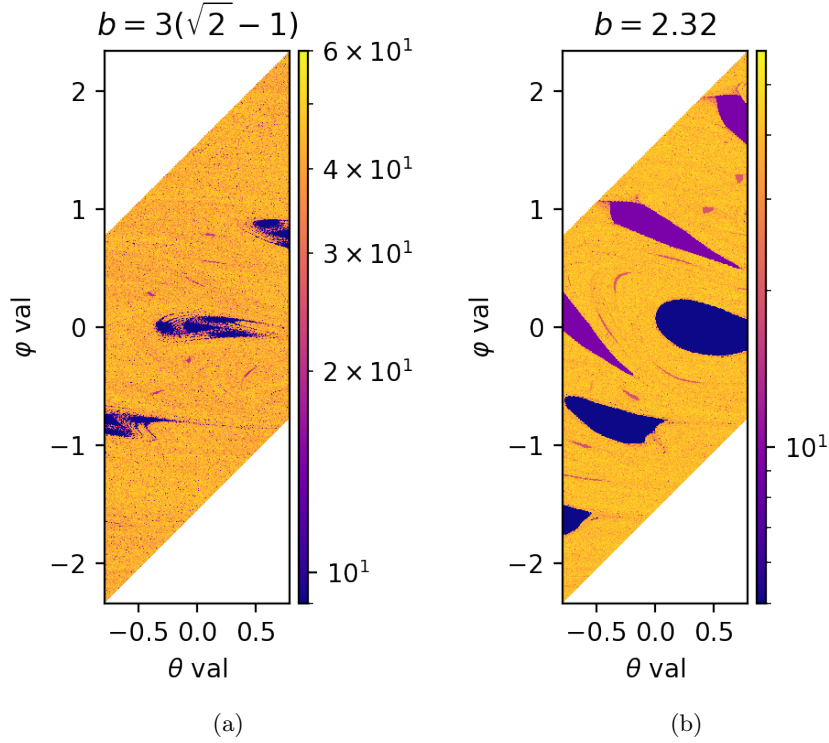

Figure 14: Another LZC plot of a few Poincaré sections

In fig. 14a we plot the same data except $b \approx 3(\sqrt{2} - 1)$, corresponding to fig. 4c. The size of the blue regions is about the same, so there should relate to the same quasi-periodic orbit. What's different in this case is the pronounced teardrop with fractal-like structure. If we were to iterate deeper, it looks like the fractal branches would connect to make 4 disjoint blue blobs. Around the main big region, we see smaller red specks, suggesting another quasi-periodic trajectory that we didn't expect before.

In fig. 14b, $b = 2.32$, the kind of quasi-periodicity here should be similar to 7a, 6a, and 5b. It's plausible there are 3 different quasi-periodic regions here, since you can separate the blobs easily into three sets: blue along the bottom, purple along the top, and small red in between.

4 Levy Flights

5 Conclusion

References

[Coo93] I. D. Coope. Circle fitting by linear and nonlinear least squares. *Journal of Optimization Theory and Applications*, 76:381–388, Feb 1993. `https://doi.org/10.1007/BF00939613`.

[Eva98] Lawrence C. Evans. *Partial Differential Equations*. American Mathematics Society, 1998. Providence, RI.

[Gas21] Sean Gasiorek. On the dynamics of inverse magnetic billiards. *Nonlinearity*, 34(3):1503–1524, mar 2021. `https://doi.org/10.1088%2F1361-6544%2Fabe2f1`.

[Kna18] Andreas Knauf. *Mathematical Physics: Classical Mechanics*. Springer Berlin, Heidelberg, mar 2018. `https://doi.org/10.1007/978-3-662-55774-7`.

[KS87] Kaspar and Schuster. Easily calculable measure for the complexity of spatiotemporal patterns. *Physical review. A, General physics*, 36 2:842–848, 1987.

[KS17] Andreas Knauf and Marcello Seri. Symbolic dynamics of magnetic bumps. *Regular and Chaotic Dynamics*, 22(4):448–454, jul 2017. `https://doi.org/10.1134%2Fs1560354717040074`.

[LZ76] A. Lempel and J. Ziv. On the complexity of finite sequences. *IEEE Transactions on Information Theory*, 22(1):75–81, January 1976.

[MR19] P. Mediano and F. Rosas. When and how to use Lempel-Ziv complexity. 2019. `https://information-dynamics.github.io/complexity/information/2019/06/26/lempel-ziv.html`.

[Pö82] Jürgen Pöschel. Integrability of hamiltonian systems on cantor sets. *Communications on Pure and Applied Mathematics*, 35(5):653–696, 1982. `https://onlinelibrary.wiley.com/doi/abs/10.1002/cpa.3160350504`.

[Ser22] Marcello Seri. *Hamiltonian Mechanics*. AMS Open Math Notes, mar 2022. `https://www.ams.org/open-math-notes/omn-view-listing?listingId=110861`.